Rock Mechanics and Rock Engineering (2018) 51:1995–2014
https://doi.org/10.1007/s00603-018-1444-y

ORIGINAL PAPER

Comparison of Short-Term and Long-Term Creep Experiments in Shales and Carbonates from Unconventional Gas Reservoirs

Fatemeh S. Rassouli[1] · **Mark D. Zoback**[2]

Received: 30 January 2017 / Accepted: 20 February 2018 / Published online: 8 March 2018

Abstract
We carried out a series of long-term creep experiments on clay- and carbonate-rich shale samples from unconventional gas reservoirs to investigate creep over both relatively short-term (4-h) and long-term (4-week) periods. Results from each set of experiments were compared to evaluate the ability to predict the long-term behavior of reservoir rocks using relatively short-term creep experiments. The triaxial deformation experiments were performed in a time-cycling pattern, which included a series of four stages of loading, creep, unloading and recovery experiments conducted over different time spans. The loading conditions (tens of MPa) reflect current reservoir conditions and were far below the strength of the samples. Experiments were conducted on both horizontal and vertical shale samples to address anisotropy introduced by the bedding. A power-law model was fitted to the creep data to predict the long-term behavior of shale samples. Regardless of the applied loading history, results of the experiments show that the shale samples follow a single trend representing their creep behavior through time. We show that the simple power-law model is capable of describing creep over multiple time periods. Additionally, the value of the creep compliance factor is consistent over different creep testing periods and it is possible to characterize the behavior of these samples from relatively short-term (1 day) creep experiments.

Keywords Gas shale · Elasticity · Viscoplasticity · Creep · Time-cycling creep test

1 Introduction

Low-temperature viscoplastic deformation of sedimentary rocks affects their mechanical and flow properties (Cuisiat et al. 2002; Van Oort 2003; Zhang et al. 2007; Chang and Zoback 2010; Sone and Zoback 2013; Ferrari and Laloui 2013). This time-dependent deformation leads to a more isotropic stress field. In other words, the least principal stress is expected to increase in more viscoplastic rocks, potentially creating frac barriers. Understanding variations of the least principal stress at different depths and plays helps to optimize drilling and hydraulic fracturing processes and avoid fractures growing out of zone in unconventional reservoirs (Sone and Zoback 2014b; Yang et al. 2015; Yang and Zoback 2016).

Most previous laboratory studies of viscoplastic deformation in sedimentary rocks have been carried out via uniaxial and triaxial creep experiments. Because of the time-consuming nature of these experiments, relatively few papers have addressed this topic (Kubetsky and Eristov 1970; Rutter 1972; Goodman 1989; Gasc-Barbier et al. 2004). A common challenge in laboratory creep studies is to know how long laboratory experiments need to be carried out to accurately determine the parameters necessary to predict rock deformation over relatively long periods of time. A large number of creep indentation studies have been conducted on various sizes of rock samples and shorter time scales than the conventional creep experiments (Gratier et al. 2009; Rassouli et al. 2009; Hyde et al. 2013). However, it is not clear if the deformation mechanisms governing the time-dependent deformation observed in indentation tests, where very high stresses cause localized rock failure around the indenter, are similar to those when intact rock samples are deformed under relatively modest stresses.

✉ Fatemeh S. Rassouli
frasouli@stanford.edu

Mark D. Zoback
zoback@stanford.edu

[1] Department of Geophysics, Stanford University, 397 Panama Mall, B59, Stanford, CA 94305, USA

[2] Department of Geophysics, Stanford University, 397 Panama Mall, 347, Stanford, CA 94305, USA

In this study, we carried out a series of creep experiments on shale samples with various amounts of carbonate and clay to investigate the creep parameters obtained in loading steps ranging from several hours to several weeks (time-cycling creep experiments). Our goal was to find the possibility of characterizing creep behavior of shales from short-term conventional creep tests. Here, we extend the short-term (several-hour) creep experiments reported by Sone and Zoback (2014b), where they investigated the role of clay and organic content on viscous deformation of shales from unconventional gas reservoirs. In this paper, we report a series of time-cycling creep experiments carried out on carbonate and shale rocks to test whether measurement of creep parameters from short-term tests can be used to predict long-term behavior. Sone and Zoback (2014b) showed that the time-dependent deformation of the shales was directly related to the clay and organic content. They also noted some creep deformation in samples with higher amounts of carbonates, which we investigate more thoroughly in this paper. After presenting experimental data, we analyze it in the context of a power-law creep. Finally, we briefly discuss some of the probable sources of creep in carbonate-rich shales based on microscopic images.

2 Experimental Methods

In this study, we performed a series of triaxial creep experiments on clay-rich samples from the Haynesville formation in northwest Louisiana and east Texas and carbonate samples from the Eagle Ford formation in South Texas to investigate the viscoplastic deformation processes in shales. All the experiments were conducted at room temperature. Loading was carried out in a time-cycling pattern on samples oriented either parallel or perpendicular to bedding planes to document anisotropy effects. This time-cycling pattern includes a series of multi-stage loading and unloading experiments at different time spans as is discussed in the following sections.

2.1 Geology of the Studied Regions

The Eagle Ford Shale is late Cretaceous in age and is located between the Buda limestone below and the Austin chalk above. Because of the extremely low permeability of the Eagle Ford formation, horizontal drilling and hydraulic fracturing are required to extract oil and gas from these resource rocks (Mullen 2010; Fan et al. 2011). The samples we used in this study come from the middle zone of the formation, where the gas production occurs and the thickness of the Eagle Ford formation is relatively high. Mineralogy of the Eagle Ford formation varies significantly, but the part located in the gas window of the formation is laminated with a composition rich in carbonates and quartz (Mullen 2010; Fan et al. 2011). The overburden stress gradient for Eagle Ford upper samples is estimated to be 24 MPa/km in the middle gas window of the formation. The horizontal stresses at depths of 3.84–3.87 km that our samples are from are approximately 50–75 MPa, while the vertical stress is estimated to be about 92 MPa (from Lund Snee and Zoback 2016).

The Haynesville formation is located between north Louisiana and east Texas. Similar to the Eagle Ford formation, Haynesville shale gas was discovered as a commercial formation in 2007 owing to hydraulic fracturing and horizontal drilling processes. A part of the Haynesville formation located in Mississippi and northern Louisiana is more of the siliciclastic type of shale, while the part located on the western side of Louisiana and east Texas is organic-matter-rich shale. The texture and microstructure of the Haynesville, being a heterogeneous mudstone, is controlled by various factors such as alignment of the illitic clay-dominated matrices and distribution of organic matter (Spain and Anderson 2010; Hammes et al. 2011). The porosity of Haynesville is mostly intercrystalline microporosity located in the matrix. In silty zones and between the laminates, porosity is observed in the form of intergranular porosity (Spain and Anderson 2010). The pressure gradient in Haynesville formation reaches up to 20.4–22.5 MPa/km (Thompson et al. 2011; Pope et al. 2009). The Haynesville samples in this study are from a depth of 3.4 km. This means that the overburden pressure at this depth can reach up to 80 MPa. Also, around this depth the horizontal stresses are calculated to change between 40 and 80 MPa (from Lund Snee and Zoback 2016; Fan et al. 2016).

2.2 Sample Description

The mineral compositions of the samples collected from the Haynesville and the Eagle Ford formations were obtained by powder X-ray diffraction (XRD) and pyrolysis analysis, which are provided in Table 1. The analysis shows that the shale samples from Haynesville formation have more than 50% clay content, while in the samples from Eagle Ford formation, carbonates are the dominant minerals. The vertical sample "HV 35" and the horizontal sample "HH 37" were cored from the same depth in the Haynesville formation and have the same mineral compositions. Additionally, pyrolysis analysis of these samples indicates that the maturation of the organic matter in all four samples correspond to dry gas window.

To calculate the porosity of these samples, we measured the grain density (ρ_g) of the samples through helium pycnometry. Having the volumes, weights and the resulting bulk densities (ρ_b), we calculated the porosity using the following equation:

Table 1 Summary of characteristics of the samples used for triaxial creep experiments

Sample	Formation	Orientation	Carbonate (wt%)	Clay (wt%)	Quartz (wt%)	TOC (wt%)	Water content (%)	Bulk density (g/cm^3)	Porosity (%)
HV 35	Haynesville	Vertical	7	62	20	1.6	1	2.47	8.14
HH 37	Haynesville	Horizontal	7	62	20	1.6	1	2.47	8.14
EV 8	Eagle Ford	Vertical	51.27	20	16	4.73	0.3	2.45	4.34
EH 5	Eagle Ford	Horizontal	84.99	3	8	3.01	0.3	2.45	5.94

$$\phi = \frac{\rho_g - \rho_b}{\rho_g} \times 100. \quad (1)$$

The diameter of the cylindrical samples was 2.54 cm (1 in.), and their length ranged from 3.81 cm to 5.08 cm (1.5–2 in.). The cylindrical axes of these samples were chosen to be either parallel (horizontal samples) or perpendicular (vertical samples) to the bedding planes to investigate the effect of bedding plane orientation on long-term physical properties of shales (anisotropy).

Samples were tested in the "as-received" condition to best represent the in situ hydration states. Since the main goal of this research was finding an efficient method to study long-term deformation of shales, all the experiments were performed at ambient temperature (22 ± 0.5°C) and drained pore pressure conditions. The effect of reservoir temperature on creep of shales will be addressed in future studies.

2.3 Methodology of Triaxial Creep Experiments

Creep experiments were conducted in a servo-controlled triaxial apparatus. A heat-shrink Viton jacket was used to seal the samples from the mineral oil used as a confining fluid. The samples were placed between two titanium core holders inside a pressure vessel in which a constant confining pressure was applied to the samples. The experiments were conducted under room dry condition, and no fluid was flowing into the system. Drainage of the samples was possible through the two holes drilled at the center of the two core holder bases being connected to atmosphere. The piston inside the vessel applied axial differential pressure, and a pair of linear variable differential transformer (LVDT) displacement transducers with an accuracy of 0. 1 microns, attached to the core holders, measured the sample deformation in the axial direction. Radial deformation was not measured in this study; as in Sone (2012), this variable was shown to be negligible compared to axial deformation at room temperature and stresses we used in this study. The confining pressure was controlled with a feedback from a pressure transducer with a 0.05 MPa accuracy, while the axial pressure was controlled by a feedback from an internal load cell with 0.3 MPa accuracy.

We ran multi-stage creep tests over different time windows on the four samples described in Sect. 2.2. Confining pressure was increased with a rate of 4 MPa/min at the beginning of each experiment. The time-cycling creep tests consist of four individual cycles as shown in Fig. 1 for sample "HV 35." Each cycle included loading, creep (C), unloading and recovery (R) phases. Increasing or decreasing the axial differential pressure over a period of 2 min achieved loading and unloading of the samples. In contrast, the creep and recovery time, under which the stresses were kept constant, varied from 3 to 4 h (1st cycle), to 1 day (2nd cycle), to 1 week (3rd cycle) and to 1 month (4th cycle).

All triaxial tests were performed at a constant confining pressure of 40 MPa. An axial differential stress of 30 MPa was applied to "HV 35" over the creep phases. The same value of differential stress was applied to "HH 37" during the first creep cycle. But, since the deformation of "HH 37" at 30 MPa was very small, we increased the differential stress to 40 MPa and conducted the four cycles of creep at this stress level. This observation was in agreement with the results of creep experiments on samples with similar lithologies conducted by Hyde et al. (2013) and Sone and Zoback (2013), where they reported less time-dependent deformation for horizontal samples than for the vertical ones. The 40 MPa differential stress value was also used for the creep tests on the carbonate-rich samples, "EV 8" and "EH 5." The differential stresses were kept constant over all the creep phases. The stresses were chosen to be close to the reservoir in situ stresses mentioned in Sect. 2.1 to generally simulate reservoir conditions. At the end of each creep stage, the differential stress was decreased approximately to 9 MPa (Fig. 1).

Sone (2012) showed that room-dried shale samples from unconventional gas reservoirs exhibited the same time-dependent deformation as oven-dried samples. For this reason, he concluded that poroelastic effects are not a major cause of time-dependent behavior exhibited by the gas shale samples he studied. Similarly here, we assumed the poroelastic effect to be negligible for our samples with less than 1

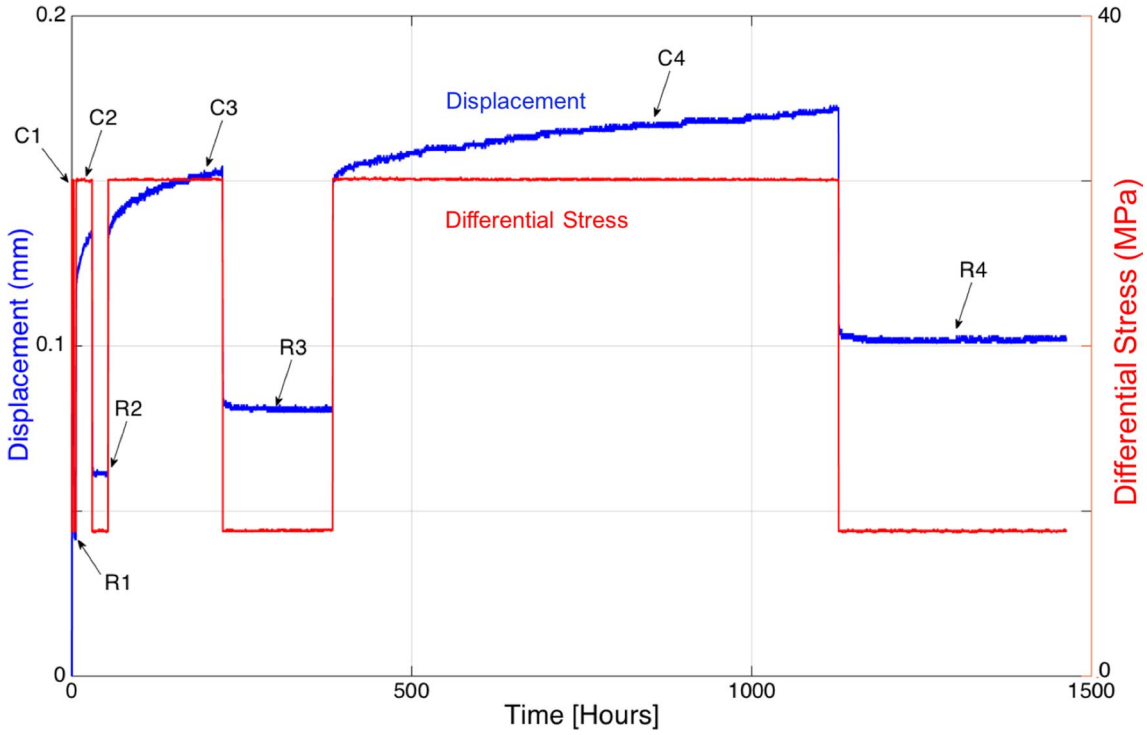

Fig. 1 Time-cycling loading and unloading triaxial creep experiment on "HV 35" as an example. *C* and *R* stand for creep and recovery stages, respectively. The differential stress for all the creep stages is equal to 30 MPa (red curve). The time-dependent deformation response of the sample is shown in blue

and 0.3% water content and porosity of 4.3–8% for clay- and carbonate-rich shales, respectively (Table 1).

3 Experimental Results

The stress–strain curves for creep experiments on the two vertical samples are presented in Fig. 2. The creep stages start where the stress level reaches the constant value of 30 MPa for "HV 35" and 40 MPa for "EV 8." Similarly, the rebound stages are where the stress level is kept constant at the lowest stress level. Young's modulus (E) values are calculated from the slope of the stress–strain curves in Fig. 2 at both loading and unloading stages, which are shown in Fig. 3.

In Fig. 3, there is a 7.5–16% difference between the Young's moduli calculated from the first loading and unloading steps, while the differences between the two values for the other steps are less than 1% for all the samples, except for the second cycle of "HH 37" with a 4% difference between the loading and unloading E values. This means that most of the deformation observed at the loading stages has been recovered elastically during the unloading stages. The significant difference between the loading and unloading E values for the first cycles is a result of the closure of microfractures initiated during exhumation, which has the greatest effect when a load is first applied to the samples. After applying a load to the samples for the first time and closing the induced microfractures, the samples behave more like in situ material. We refer to the initial loading cycle as a seasoning process to prepare the samples for the main experiments (following Brace et al. 1966; Wawersik and Brace 1971; Bernabe 1986). This seasoning process for the time-cycling tests is discussed further in Appendix 1.

4 Discussion of Creep Observations

4.1 Creep Strain Measurements

Total strain in creep experiments can be divided into three separate types of strain as shown in the following equation:

$$\varepsilon_t = \varepsilon_e + \varepsilon_p + \varepsilon_c, \tag{2}$$

where ε_t is the total strain and ε_e, ε_p and ε_c represent elastic, plastic and creep strains, respectively (Chaboche 2008).

Elastic strain is defined as the immediate recoverable deformation represented by the E magnitudes in Fig. 3, while viscoelastic strain is a time-dependent recoverable deformation of samples. Plastic deformation is considered to be an instantaneous permanent deformation of rocks, and

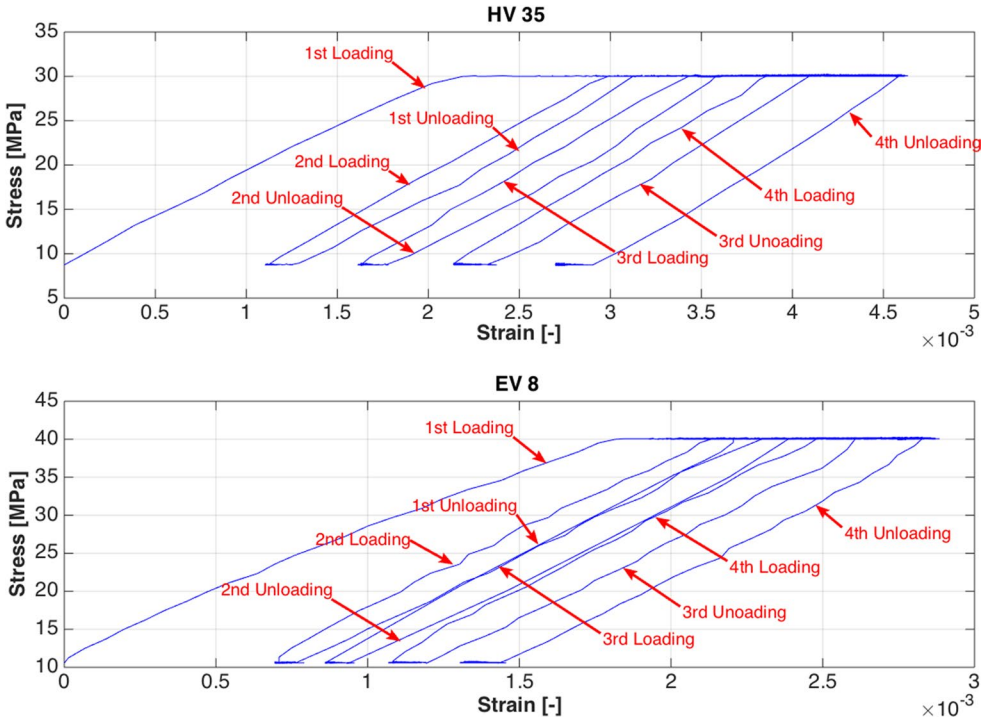

Fig. 2 Stress versus strain curves for vertical clay-rich shale, "HV 35," and vertical carbonate-rich shale, "EV 8," samples

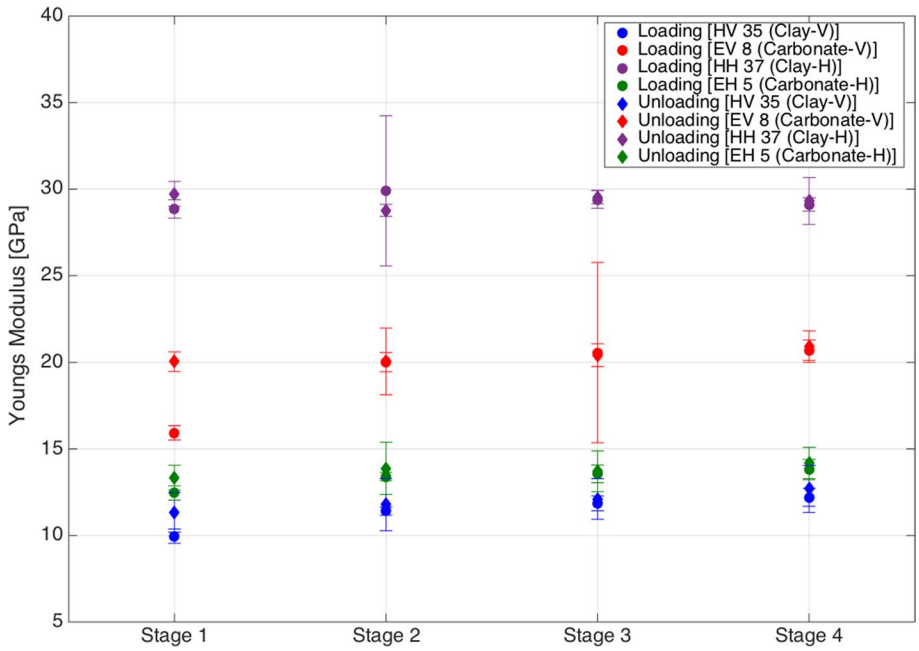

Fig. 3 Young's modulus values at different loading and unloading stages during time-cycling creep experiments. The loading and unloading E values match for each of the stages, except during stage one. The error bars indicate the 95% confidence bound of the calculated Young's moduli

viscoplastic deformation is related to the time-dependent permanent deformation of samples (Yoshida 1990; Chaboche 1986; Khan and Farrokh 2006; Krempl et al. 1986; Ruggles and Krempl 1990).

To better observe these different phases, the first two cycles of the experiment on "EV 8" are shown in Fig. 4. Here, the elastic response (ε_e) includes both instantaneous elastic and viscoelastic deformations of the rock. The irrecoverable strain ($\varepsilon_{p,c}$) of this sample at each stage can be calculated by subtracting (ε_e) from the total strain (ε_t).

The time-dependent deformation of the rock (ε^2_{TD}) includes both viscoelastic and viscoplastic (creep) deformations, which in Fig. 4 indicates the deformation of the sample from the point where the differential stress reaches 40 MPa to the first unloading point. The viscoelastic deformation shown by ε_{VE} in Fig. 4 represents the time-dependent recoverable deformation of the rock. By subtracting

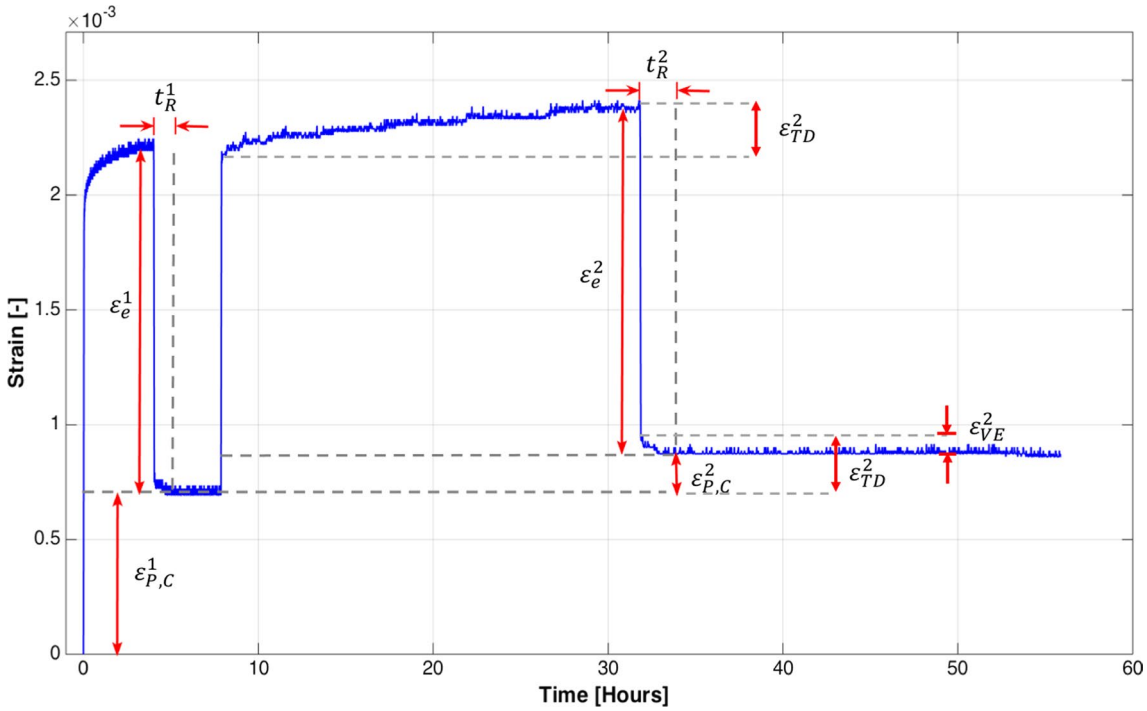

Fig. 4 Projection of elastic deformations, ε_e, permanent deformations, $\varepsilon_{p,c}$, and rebound time, t_R, for the first two cycles of creep experiment on vertical carbonate-rich shale sample, "EV 8"

ε_{VE} from ε_{TD}^2, we can calculate the creep deformation of the sample, which is equal to $\varepsilon_{p,c}$ for steps two to four. As a result, most of the permanent accumulated strain during the cyclic loading is observed at the creep steps, but not during loading or unloading stages for these cycles, which is in agreement with Yoshida (1990). At the same time, most

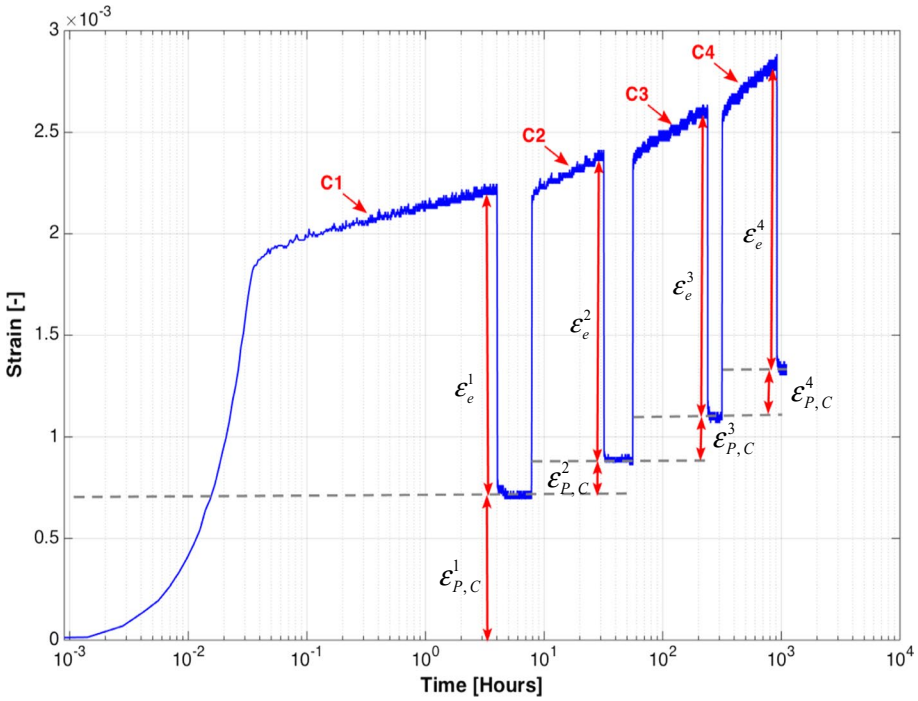

Fig. 5 Semi-log plot of strain as a function of time for the time-cycling creep test conducted on "EV 8." $\varepsilon_{P,C}^2$, $\varepsilon_{P,C}^3$ and $\varepsilon_{P,C}^4$ are in the range of $[0.22 \times 10^{-3}, 0.24 \times 10^{-3}]$

of the instantaneous plastic deformation occurs at the first cycle within $\varepsilon^1_{P,C}$.

Figure 5 shows all of the cycles of this experiment in a semi-log time versus strain plot. This plot gives an overview of the different types of deformations during the four loading cycles. The permanent strain of rock in the second, third and fourth stages ($\varepsilon^2_{p,c}$, $\varepsilon^3_{p,c}$, $\varepsilon^4_{p,c}$) is about 3×10^{-4}, although the required time to obtain $\varepsilon^4_{p,c}$ (4 weeks) is longer than those required for $\varepsilon^3_{p,c}$ (1 week) and $\varepsilon^2_{p,c}$ (1 day), meaning that the creep strain rate decreases rapidly with time (also see Sone and Zoback (2014b)). For this reason, one would expect a finite amount of creep strain, even after very long periods of time.

Here, the time window that the deformation recovery reaches a stable value is named "rebound time." The rebound times (t^1_R and t^2_R) shown in Fig. 6 are over very short periods at the beginning of the recovery steps and are very small compared to the rest of their corresponding stage recovery time. These rebound periods get longer as the creep duration increase from few hours to 4 weeks.

To study the total creep of samples, first we measured the inelastic deformation of each stage. To do so, we denote each cycle's number "m". If we remove the initial data of the mth creep stage in a time window equal to the mth rebound time, t^m_R, the remainder creep data will be equal to the inelastic deformation of the sample for each creep stage. This inelastic part of the creep deformation is referred to as "the secondary creep," which is defined in many time-dependent creep studies (Cogan 1976; Lockner and Byerlee 1977; Boukharov et al. 1995; Fujii et al. 1999).

Next, we removed the mth unloading and recovery phases in addition to the $(m+1)$th recoverable deformation. As shown in Fig. 6 for the first two loading cycles, by shifting the $(m+1)$th inelastic deformation toward the ending point of the mth inelastic deformation on the time axis, we found that the inelastic deformation of stage $m+1$ starts right at the point where the mth inelastic deformation ends. So, regardless of the loading history, the sample is following one time-dependent trend, representing its creep behavior.

This is consistent with the experiments reported by Yoshida (1990), where he showed that the amount of visco-plastic strain accumulation in creep-ratcheting experiments was almost the same as that in a single static creep test at a given total hold time. Figure 7 shows all the calculated inelastic deformations attached as one graph for "EV 8." Total strain amounts for all the other samples are presented in Appendix 2.

4.2 Power-Law Creep Model

Sone and Zoback (2013) performed a series of triaxial creep experiments on samples from different shale formations with diverse compositional properties. Each of these triaxial creep data sets was collected over 3-h and 2-week time spans and at different applied differential stresses. A power-law

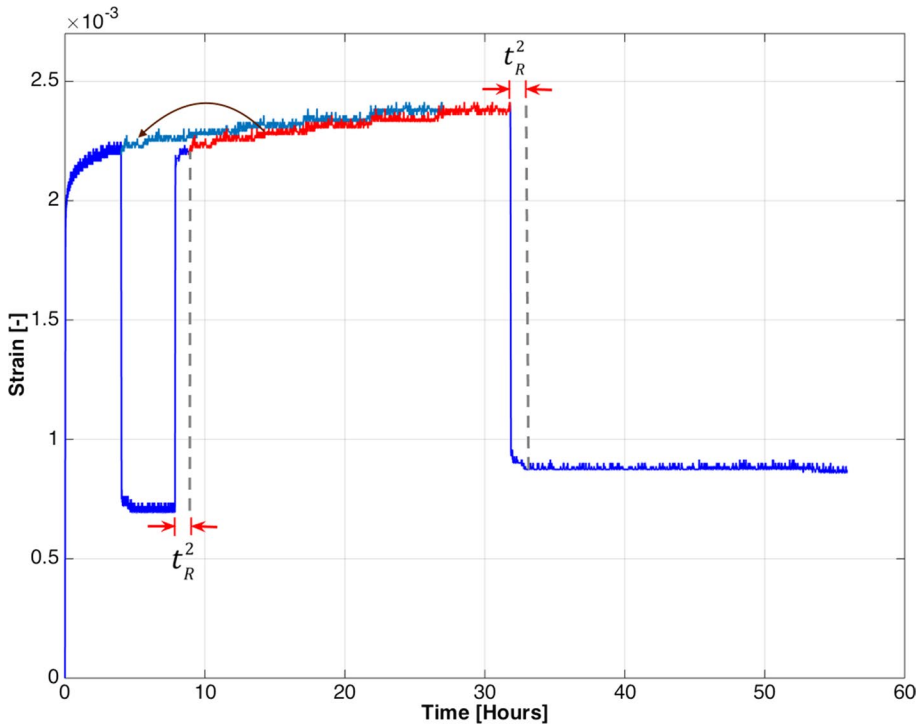

Fig. 6 Attaching the first creep point of the second stage to the last creep point of the first stage for "EV 8." The second creep deformation is continuing the first one

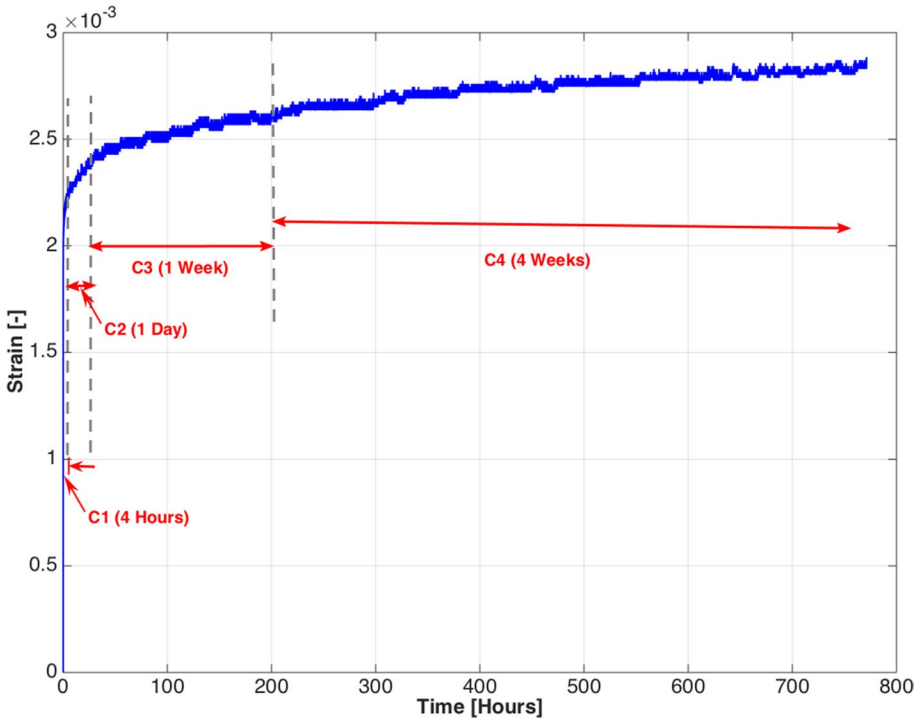

Fig. 7 Total creep strain of sample "EV 8," after attaching all the inelastic responses. This total creep is irrespective of the cyclic loading history

function of time (t) was found to be the best model fitting the triaxial creep data. The model is of the following form:

$$\varepsilon = \sigma \times Bt^n \tag{3}$$

$$J = \frac{\varepsilon}{\sigma} = Bt^n, \tag{4}$$

where ε is strain, σ is the differential applied stress (axial stress minus confining pressure), B and n are empirical constants, and J is the creep compliance factor. The constant parameters n and B can be determined from laboratory data by fitting a straight line to the data in a $\log(\text{time}) - \log(J)$ space.

Results for the clay-rich sample "HV 35" and the carbonate-rich sample "EV 8" are shown in Fig. 8a, b, respectively. The intercept of the linear fit at $t = 1$ s provides the logarithm of constant B, and the slope of the linear fit provides the power exponent n. Following the approach suggested in the study by Lakes (2009), the first 100 s of data points were not considered in the regression because these data points belong to the loading stage. The lines fitted to the four creep steps of each experiment shown in Fig. 8 are almost parallel to another. This indicates that although the duration of creep phases is different, their corresponding n values are very close to each other.

The n and B values obtained from the second to fourth cycle for all of the four experiments are shown in Fig. 9. The corresponding values for the first cycle of the experiment are not plotted because the n and B values for the first cycles act as outliers due to the physical condition of the samples. As mentioned above, the samples were used in the as-received condition. Applying a load for the first time helps closure of the cracks induced by the changes in physical conditions from reservoir to the ground surface, and also drilling processes.

The B value in Fig. 9 indicates the elastic response of the samples and is proportional to the reverse of Young's modulus (Sone and Zoback 2014a), while the power n represents the viscoplastic response of the samples. The B values for each series of experiments decrease as the creep time increases showing the fact that the samples get stiffer after each creep step, which is in agreement with the results provided in Fig. 2. In this figure, the E values slightly increase after each cycle.

Figure 9 shows the effects of anisotropy and mineral composition on creep of shale samples. In general, both the n and B values of the vertical samples, "HV 35" and "EV 8," are higher than those for the horizontal samples, "HH 37" and "EH 5," meaning that the samples being loaded normal to the bedding planes are more compliant than the samples being loaded parallel to the bedding planes, although the B values of "EV 8" are slightly less than those of "EH 5." This can be a result of difference between the mineralogy of the two samples. Sone and Zoback (2014b) showed that shales with a higher amount of ductile clay minerals and organic matter have a higher porosity, which both result in compliant behavior in clay-rich shales. The high values of n and B for the vertical clay-rich "HV 35," even at a lower applied differential stress of 30 MPa, is due to the higher clay content and the bedding plane orientation. The higher n value for

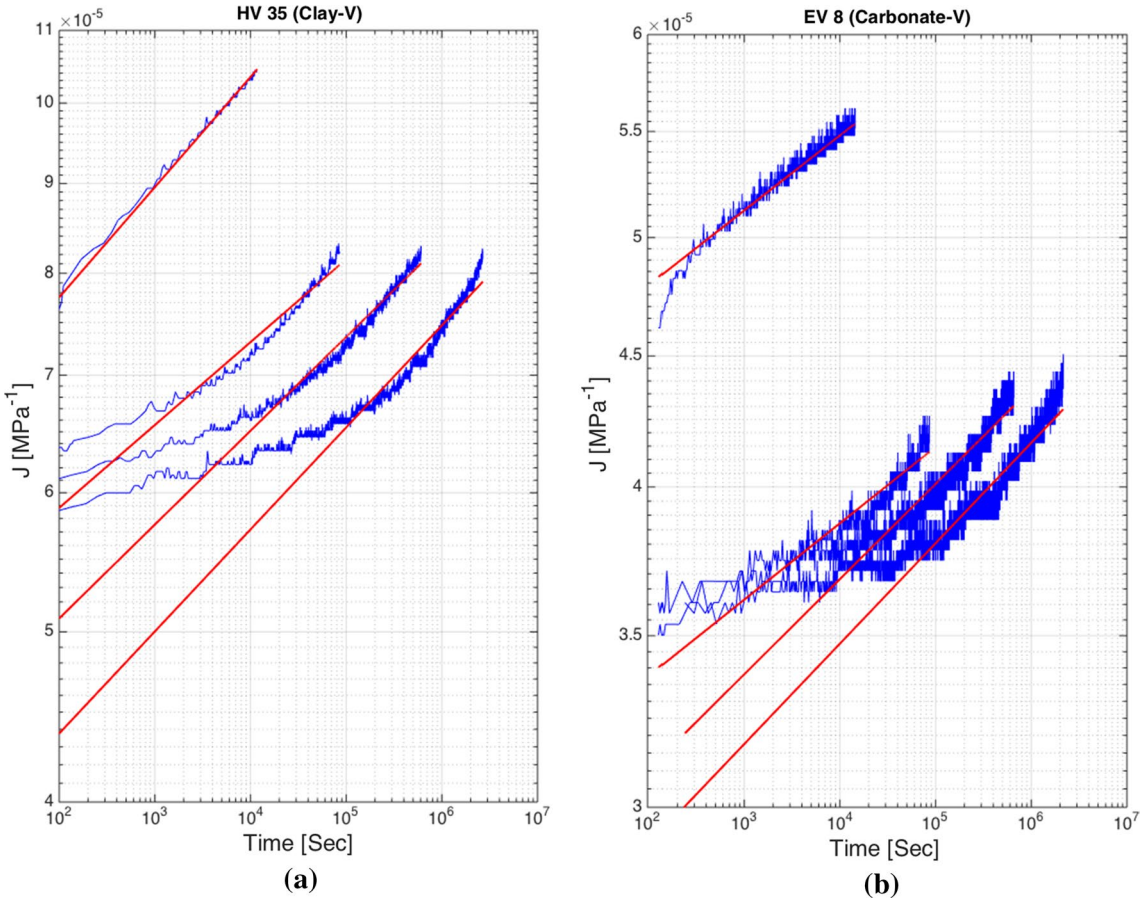

Fig. 8 Linear regression performed in a log–log space for **a** "HV 35" and **b** "EV 8" to determine the *B* and *n* constants

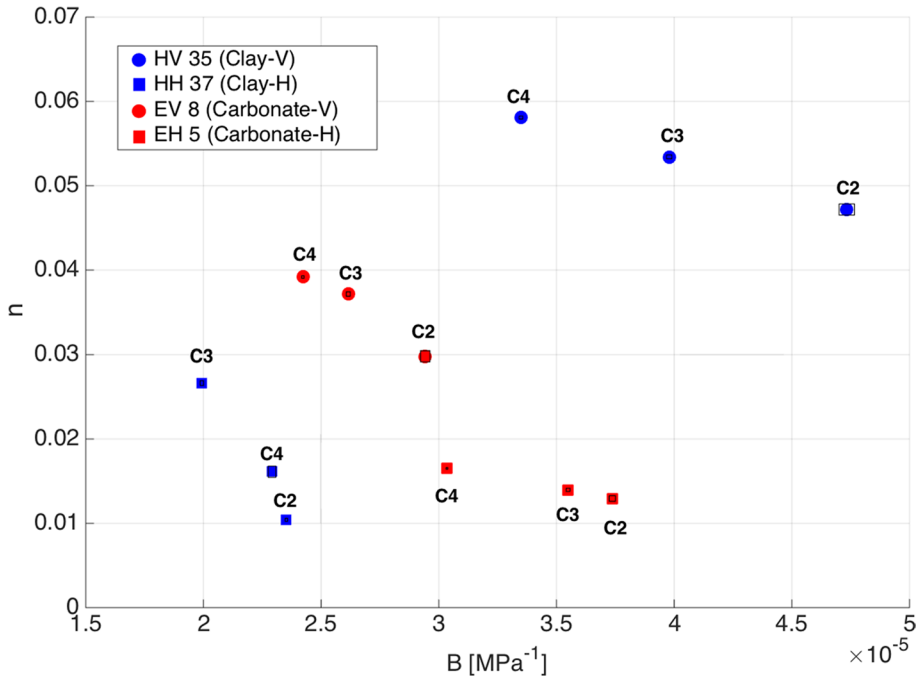

Fig. 9 *B* and *n* values calculated for C2 (1 day), C3 (1 week) and C4 (4 week). C stands for the creep stages

"EV 8" shows higher viscoplastic behavior of this sample compared to "EH 5," which is because of the bedding plane orientation, higher value of TOC in "EV 8" and higher carbonate content in "EH 5," although the porosity of "EV 8" is slightly lower than the one for "EH 5" (Table 1).

We calculated the *J* values at each stage using the provided *n* and *B* values for all the samples. These calculated values are shown in Fig. 10, where the calculated compliance factors in all the three stages are very close to each other and in a range of less than ± 10% of the average *J* value for each individual sample. Comparing the *B*, *n* and J values of samples "EH 5" and "EV 8" is quite interesting. "EV 8" has a slightly higher value of Young's modulus than "EH 5," which is unusual as Sone and Zoback (2014a, b) found samples loaded normal to bedding to have a lower Young's modulus and be more viscoplastic. However, in Fig. 10 we see the value of the importance of the constitutive model we are using—because viscoplastic deformation is not simply inversely proportional to Young's modulus, sample "EV 8" is characterized by greater viscoplastic deformation because of the high of *n*.

The Haynesville samples exhibit higher degrees of anisotropy compared to the Eagle Ford samples. The 30% difference between Young's moduli of "HV 35" and "HH 37" presented in Fig. 3 indicates elastic anisotropy of the Haynesville samples. Sone and Zoback (2013) discussed that samples with elastic anisotropy show anisotropic creep behavior. From their work, the higher amounts of inelastic deformation of the vertical sample "HV 35" compared to the horizontal "HH 37" are clearly related to the bedding planes. In the samples with high clay content, lamination caused by orientations, shape and distribution of matrix clay and organic matter is the main source of fabric anisotropy (Horsrud et al. 1998; Li et al. 2015). Ductile creep and brittle strength of shale gas rocks are controlled by their material composition and sample anisotropy. Although creep deformation increases with increasing clay and organic content, it is also strongly controlled by the direction of loading with respect to the sample orientation. Additionally, elastic strength and peak strain of clay-rich vertical samples are higher than the horizontal ones (Sone 2012; Rybacki et al. 2015). Applying the differential load orthogonal to the bedding planes causes mechanical compaction by closing bedding planes and microfractures in rocks. Also, the laminated nature of clay platelets embedded within the bedding planes

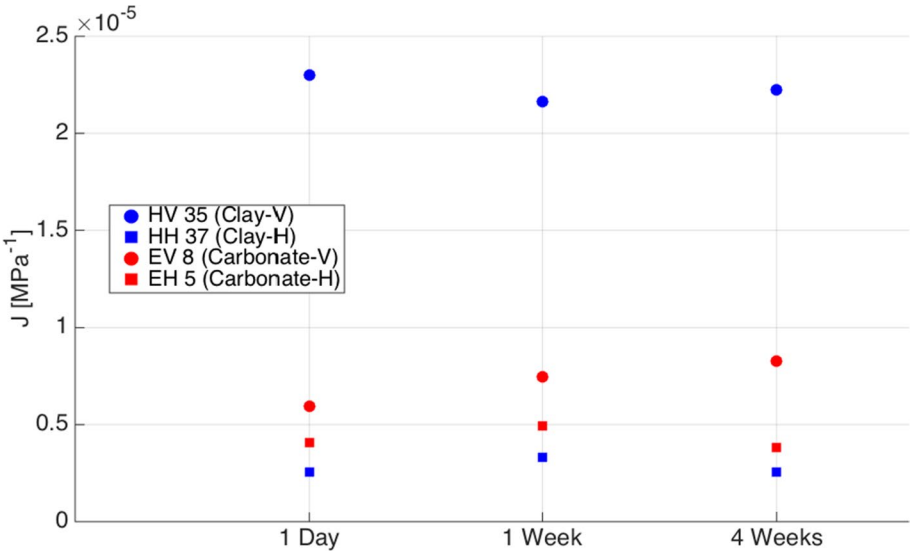

Fig. 10 Creep compliance factor at different creep stages for all of the four samples

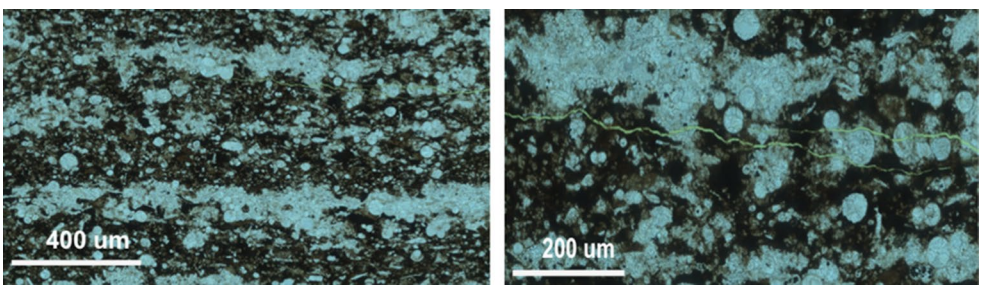

Fig. 11 Light microscopy images from "EH 5." Microfractures follow the bedding plane trend

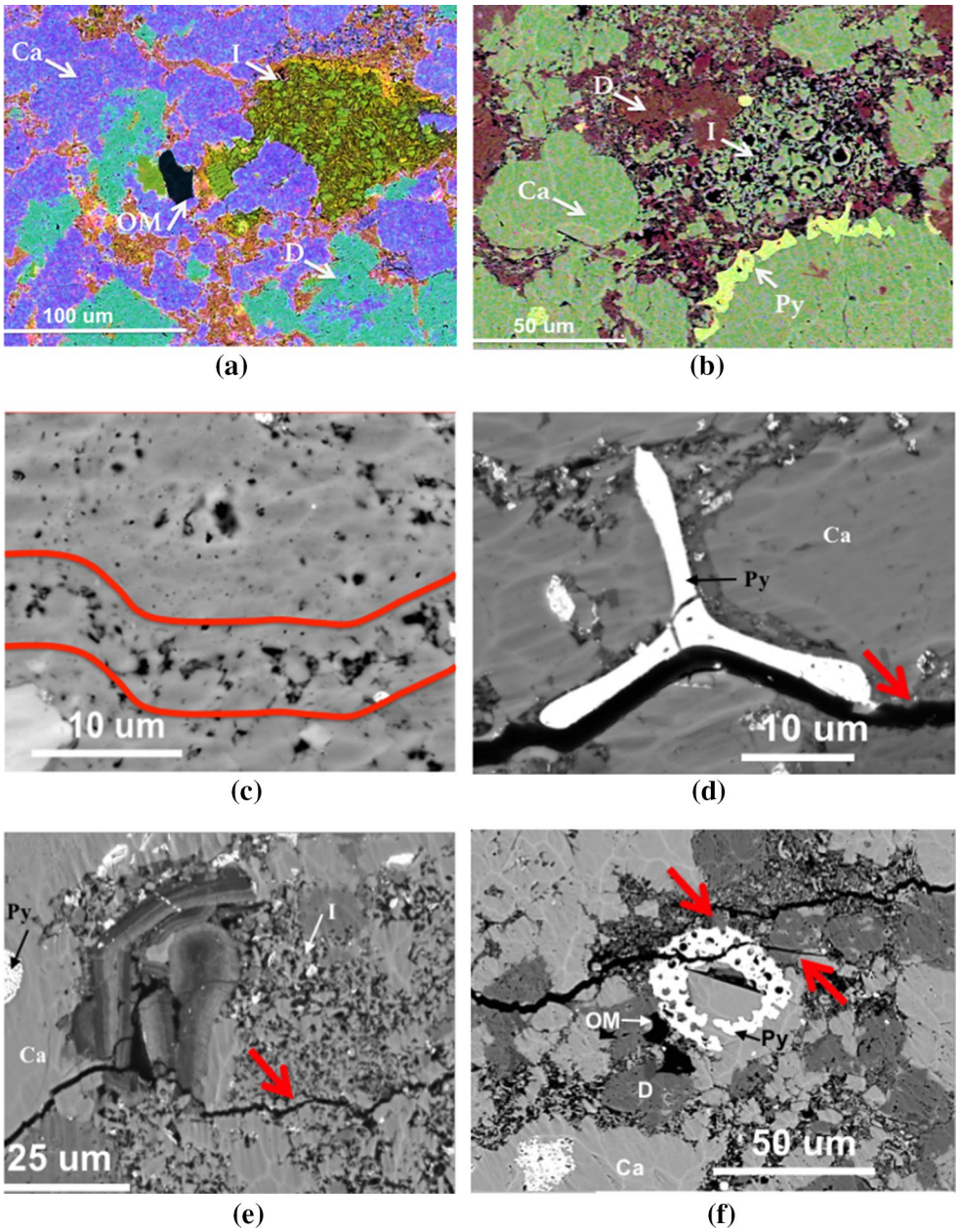

Fig. 12 EDS maps of sample EV 7 **a**, **b** (I) clay minerals, (D) dolomite, (Ca) calcite, (OM) organic matter and (Py) pyrite; **c** porous nature of dolomite grains. The red lines show a physically weak band in the dolomite grain as a result of pore connections; **d**–**f** microfractures located at the interface between different minerals. All of these microfractures are filled with organic matter. The microfractures in (**f**) have dissipated in high-porosity and clay regions

increases the deformation of the vertical samples (Kwon et al. 2004; Bayuk et al. 2007).

The presence of carbonates in the Eagle Ford samples as a cementing part in shales increases the stiffness of these rocks compared to the clay-rich samples (Kias et al. 2015). For this reason, the creep compliance of the Eagle Ford samples in Fig. 10 is less than 10^{-5} MPa^{-1}. Similar to the Haynesville shales, the anisotropy of these rocks caused by the presence of the small amount of clay and bedding orientation made the vertical "EV 8" more viscoelastic than the horizontal "EH 5."

A comparison between dynamic Young's moduli and anisotropy effects on elastic responses of the sample during the cyclic creep experiments is presented in Appendix 3.

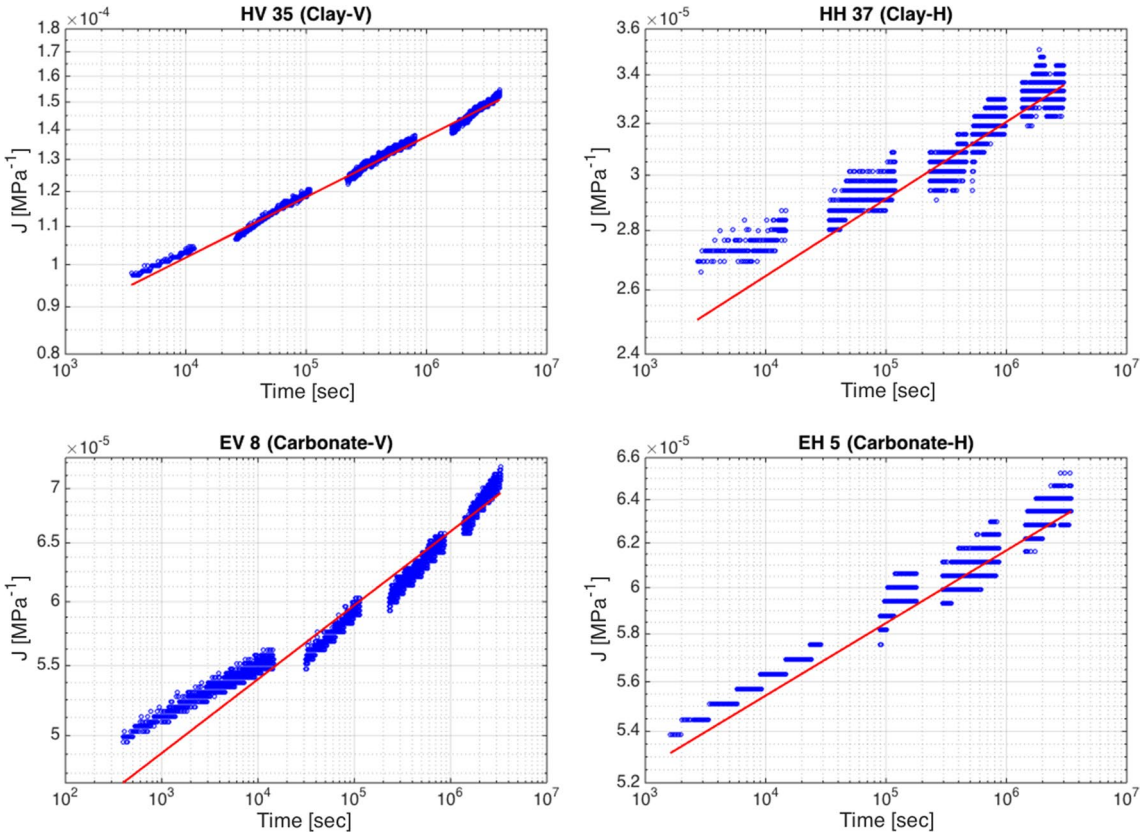

Fig. 13 Linear regression performed in a log–log space for all the samples

4.3 Sources of Creep

Besides the change in porosity and organic matter as sources of creep in clay-rich shales, the presence of clay-bound water at room temperature affects time-dependent deformation of clay-rich shale samples. This small water content facilitates grain sliding by decreasing the frictional coefficient between clay platelets and the frictional coefficient of the interface between clays and other minerals (Moore and Lockner 2004).

At temperatures below 150 °C, mechanical compaction (accommodated through pore collapse), grain sliding and pressure solution are principally responsible for time-dependent deformation of carbonate-rich shales (Croizé et al. 2013; Zhu et al. 2010; Paterson and Wong 2005). Mechanical twinning, cataclastic deformation, shear-enhanced compaction and propagation of microfractures also contribute to near-perfect plastic deformation at crystal-to-crystal boundaries at temperatures of hydrocarbon reservoirs (Yoshida 1990; Kennedy and White 2001; Paterson and Wong 2005; Davis et al. 2008; Croizé et al. 2013).

Using light microscopy and scanning electron microscope (SEM) images, we tried to explore the possible sources of deformation in carbonate-rich samples from Eagle Ford formation. Further imaging analysis will be reported in our future work to expand our primary conclusions here.

We prepared thin sections of a vertical carbonate-rich sample drilled from material adjacent to sample "EH 5." Figure 11 shows the images we acquired using an Axio Imager light microscope. In this figure, lighter grains (mostly calcite) and dark matrix (dolomite, silicates, clays and organic matter) indicate high degree of lamination in the sample. Also, preexisting fractures between bedding planes are shown in green fluorescent in Fig. 11. The bedding planes and the fractures within them are the main sources of creep anisotropy in the vertical samples.

We used backscattered electron (BSE) filter to take images using an Auriga SEM and energy-dispersive X-ray spectroscopy (EDS) mapping to identify the mineral composition of the sample. Figure 12 shows some of these images. From the EDS maps (Fig. 12a, b), the sample is mostly composed of dolomite and calcite.

Dolomite grains in this sample are porous with pore sizes ranging from few nanometers to the order of tens of microns as shown in Fig. 12c. The porous nature of these dolomite grains is as a result of coupled dissolution–precipitation processes (Murray 1960; Raufaste et al. 2011; Putnis and Putnis 2007; Ruiz-Agudo et al. 2014). The ultimate strength of the

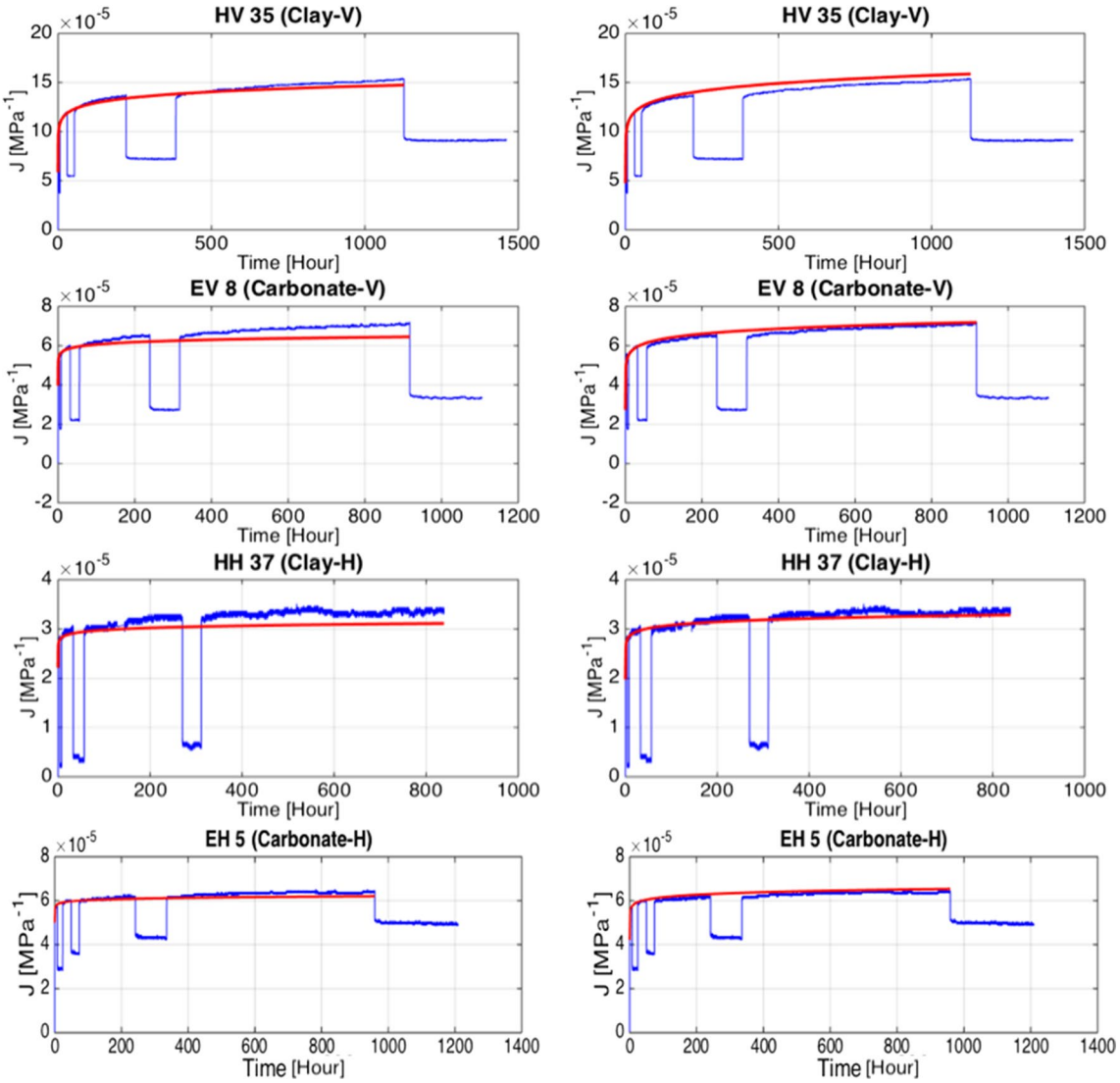

Fig. 14 Power-law equation fitted over the creep data for three different samples. The left column shows the model calculated from few-hour creep tests. The right column provides power-law model calculated from the second cycle being fitted over the data

dolomite grains has a negative correlation with porosity as described in a study by Hatzor and Palchik (1998), where they showed that this value drops from 350 to 50 MPa as the porosity increases from about 3 to 20%. In the presented case, the porosity is not uniformly distributed within the dolomite grains. The connection of larger pores creates weak porous bands within the dolomite grains (as shown with red bounds in Fig. 12c). These weak porous bands are one of the possible sources of time-dependent deformation in these Eagle Ford samples.

From the BSE images in Fig. 12d–f we observe that microfractures mostly follow the interface between two different minerals or between matrix and grains, and dissipate in organic matter or high-porosity regions. EDS maps show that these microfractures are filled with ductile organic matter and apatite. Upon applying the load to the samples, time-dependent slip over these fracture planes causes creep deformation in carbonate-rich shales.

The sources of creep for carbonate-rich shales discussed here are based on electron microscope images of two Eagle Ford samples. Further investigations on images of carbonate-rich samples from other unconventional reservoirs are needed to fully understand the sources of time-dependent deformation in these rocks.

4.4 Optimizing Creep Test Procedures

To find the minimum required time to obtain the constant parameters in Eq. 3, we fitted the power-law model to the

four stages of all the cycling experiments (Fig. 13). For samples "HV 35" and "EH 5," the fitted red line covers all stages from C1 to C4, meaning that the n and B constants for the few-hour creep test are a reasonable approximation for the long-term creep of these samples. For "HH 37" and "EV 8," it is the 1-day creep experiment giving a reasonable estimate of the long-term creep of the samples.

To better illustrate this, we calculated the n and B values for individual creep steps noting the fact that most of the elastic deformation occurred during the first cycle of the experiments as shown in Fig. 5. The mth constant parameters must be calculated while considering all of the creep steps prior to it. In Fig. 14, we fit the power-law equation calculated from the few-hour creep tests (in red) over the whole data (in blue) in the left column and compared it to the power-law equation calculated from the 1-day creep tests in the right column.

From this figure, the power-law models calculated from n and B values for the 1-day creep experiment (right column) fit the entire data set better than those calculated from the few-hour creep experiments. In other words, the 1-day creep test gives reasonable estimates of the long-term creep behavior of the rock samples. Furthermore, this figure shows that the simple power-law model is capable of describing creep curves over different time periods.

Overall, we suggest running a short creep cycle (a few hours) for "seasoning" process, before performing the 1-day experiment to obtain more reliable data. The obtained power-law equation obtained from the second cycle will be capable of predicting long-term creep of shale samples.

5 Conclusions

We performed a series of time-cycling creep experiments on shale samples obtained from the Haynesville and Eagle Ford formations. Triaxial creep experiments were conducted on both vertical and horizontal samples to address anisotropy. The samples follow the same creep behavior through multiple loading cycles over very different time spans. If we disregard the 3-to-4-h step, a power-law model with two parameters (n and B) fits the data well, regardless of the history of cyclic loading. Comparison of the n and B values among all of the creep experiments showed that both B and n are higher for the vertical samples than the horizontal ones with similar mineralogies, which shows the direct effect of sample anisotropy on long-time deformation of shale samples. However, for the carbonate-rich shales studied in this paper, the B values for the horizontal sample were slightly higher than those for the vertical sample, while the overall time-dependent deformation of the vertical sample was higher than the horizontal samples, similar to clay-rich samples.

Furthermore, we demonstrated that performing creep tests over different time periods yields consistent values of the creep compliance factor. Our study shows that although several-hour creep tests are capable of predicting the time-dependent deformation of gas shales, the 1-day creep test (after running a few-hour creep experiment to "season" samples) yields more reliable results. The parameters measured from 1-day creep experiments give a reasonable understanding of the long-term behavior of shales and help to avoid running time-consuming creep experiments.

Acknowledgements We thank ConocoPhillips and BP for providing the samples we used in this study and Carl Zeiss Microscopy for providing the imaging tools. We also thank the reviewers for the constructive comments, which helped to improve the manuscript. Financial support for Fatemeh Rassouli was provided by Stanford Rock and Borehole Geophysics (SRB) industrial consortium.

Appendix 1: Seasoning Effect

To study the behavior of the first creep cycles reported in Figs. 2, 3 and 14, we conducted a series of cyclic experiments on six different samples from Haynesville and Eagle Ford formations. The majority of the samples had a high amount of carbonate content. The mineral compositions of these samples are compared to the four samples described in the text in Fig. 15.

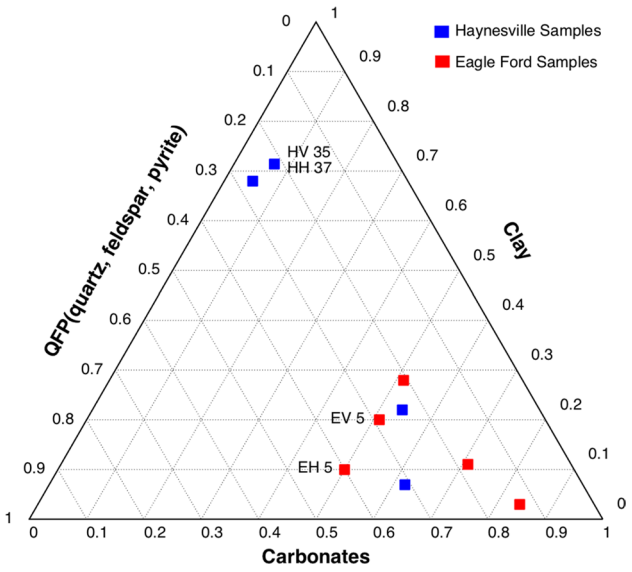

Fig. 15 Ternary plot of the composition of the samples used in cyclic experiments. The mineralogy of these samples (shown with squares) is compared to those of the samples used in time-cycling tests (diamond symbols)

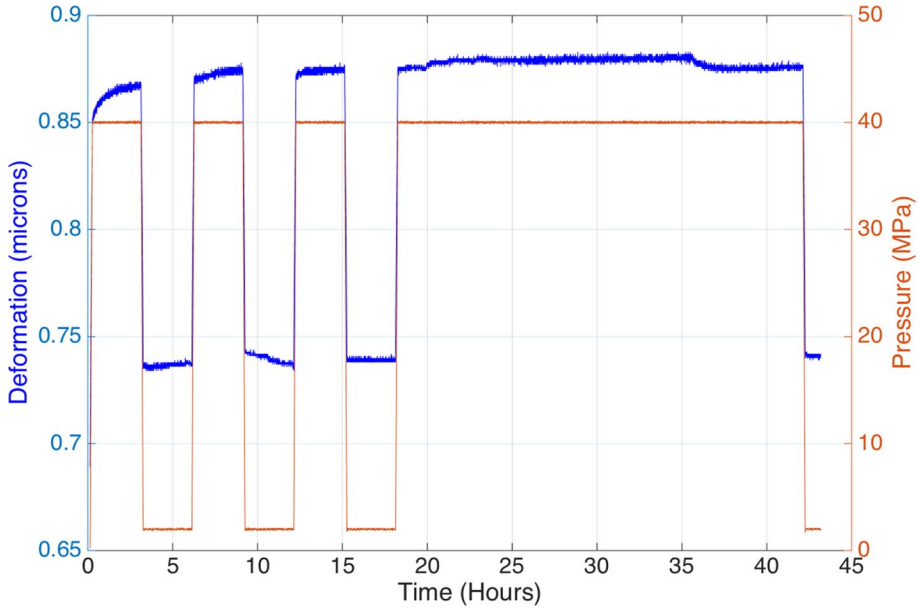

Fig. 16 Loading and unloading triaxial creep experiment on "EV 7-5" to study the seasoning effect. The differential stress for all creep stages is equal to 40 MPa (red curve). The deformation response is shown in blue

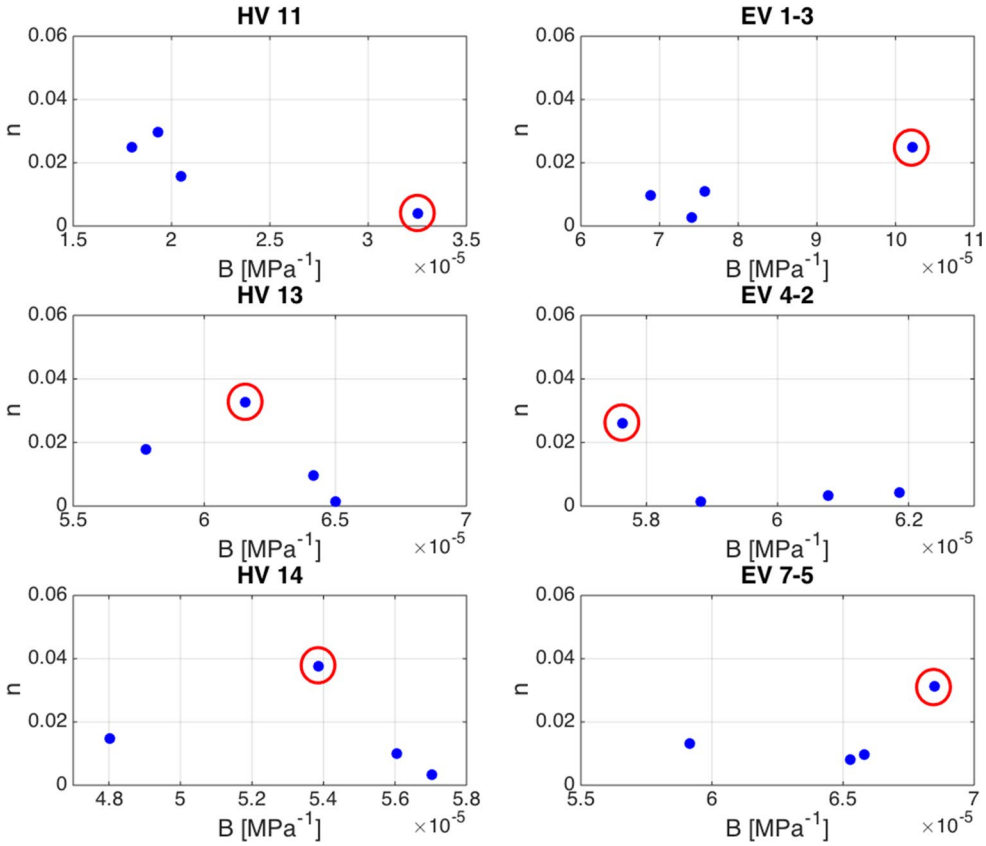

Fig. 17 n and B values calculated for six different samples from Haynesville and Eagle Ford formations. The red circles show the constant values for the first cycle of the experiments. These points are outliers

These experiments followed the seasoning process of the samples discussed in studies by Brace et al. (1966), Bernabe (1986) and Wawersik and Brace (1971), where the sample is first loaded to allow for the sample to come into a consistent position in the loading frame. The main goal of running these experiments was to compare the behavior of the first creep cycle to the rest of the cyclic stages in our protocol. This initial loading step allows slight variations in response, resulting from small heterogeneities in the sample associated with recovery, sample preparation, and loading to be

removed. After the seasoning cycle, the sample behaves more like the material in situ.

Here, we examined the seasoning process tests following the loading pattern used for time-cycling experiments (Fig. 16), which consists of four cycles of loading, creep, unloading and recovery stages. The time span of the first three creep stages was equal to 3 h, while the final loading stage lasted for 1 day. Similar to the time-cycling creep tests, both the confining pressure and differential creep stresses were kept constant at 40 MPa. The differential stress value was reduced to 2 MPa at the unloading steps.

The power-law parameters calculated for these experiments are shown in Fig. 17. As we expected, the n values for the first creep step of all these experiments (marked with red circles) are outliers, while the results for the other three steps are more uniform. This confirms our conclusion in Sect. 4.3 that to get a better prediction of the time-dependent behavior of the rocks within short periods of time, samples should be tested in a two-cycle pattern. The first few-hour cycle is to make the sample closer to the in situ state conditions, and the second creep cycle to calculate the n and B values for the viscoplastic behavior predictions.

Appendix 2

Total strains of all the samples using the method described in Sect. 4.1 are shown in Fig. 18. As mentioned before, regardless of the loading history, samples follow one time-dependent deformation trend.

Appendix 3

Ultrasonic velocity measurements were conducted during the creep experiments presented in this study. These values were calculated from the recorded travel time of ultrasonic waves generated by piezoelectric crystals attached to the inner surface of the core holders. The resolution of the recorded ultrasonic waves is 0.04 μs at room temperature.

P-wave and cross-polarized S-wave velocities were measured and used to calculate vertical and horizontal Poisson's ratio and E values shown in Figs. 19 and 20 from the following equations:

$$\mu = \rho V_s^2 \tag{5}$$

$$K = \rho\left(V_p^2 - \frac{4}{3}V_s^2\right) \tag{6}$$

$$\upsilon = \frac{3K - 2\mu}{2(3K + \mu)} \tag{7}$$

$$E = \frac{\rho V_s^2\left(3V_p^2 - 4V_s^2\right)}{V_p^2 - V_s^2}, \tag{8}$$

where E, K and μ are elastic, volumetric and shear moduli, respectively; V_s and V_p are S-wave and P-wave velocities; and ρ is bulk density.

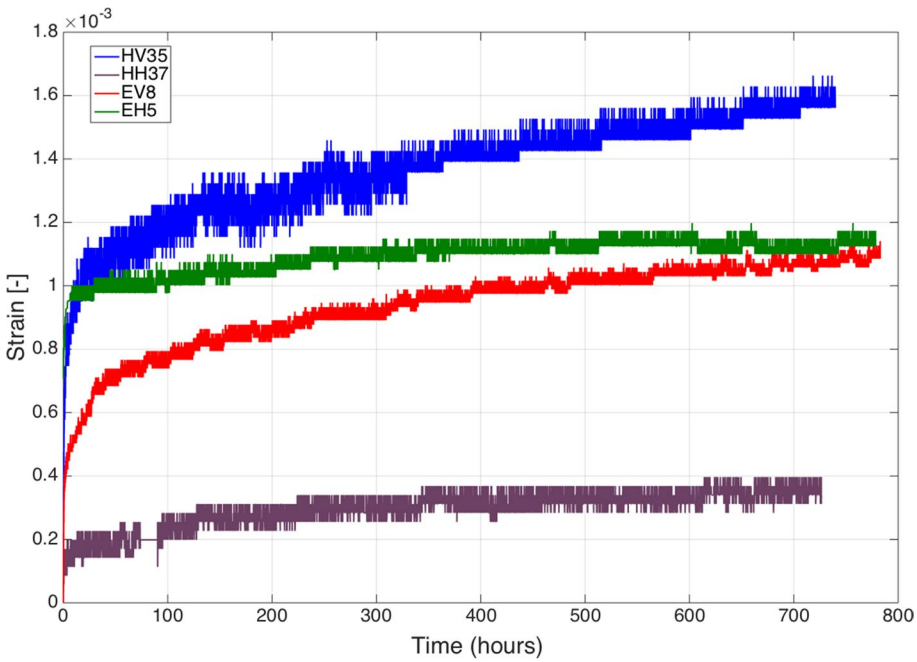

Fig. 18 Total creep strain after attaching all the inelastic responses. This total creep is irrespective of the cyclic loading history

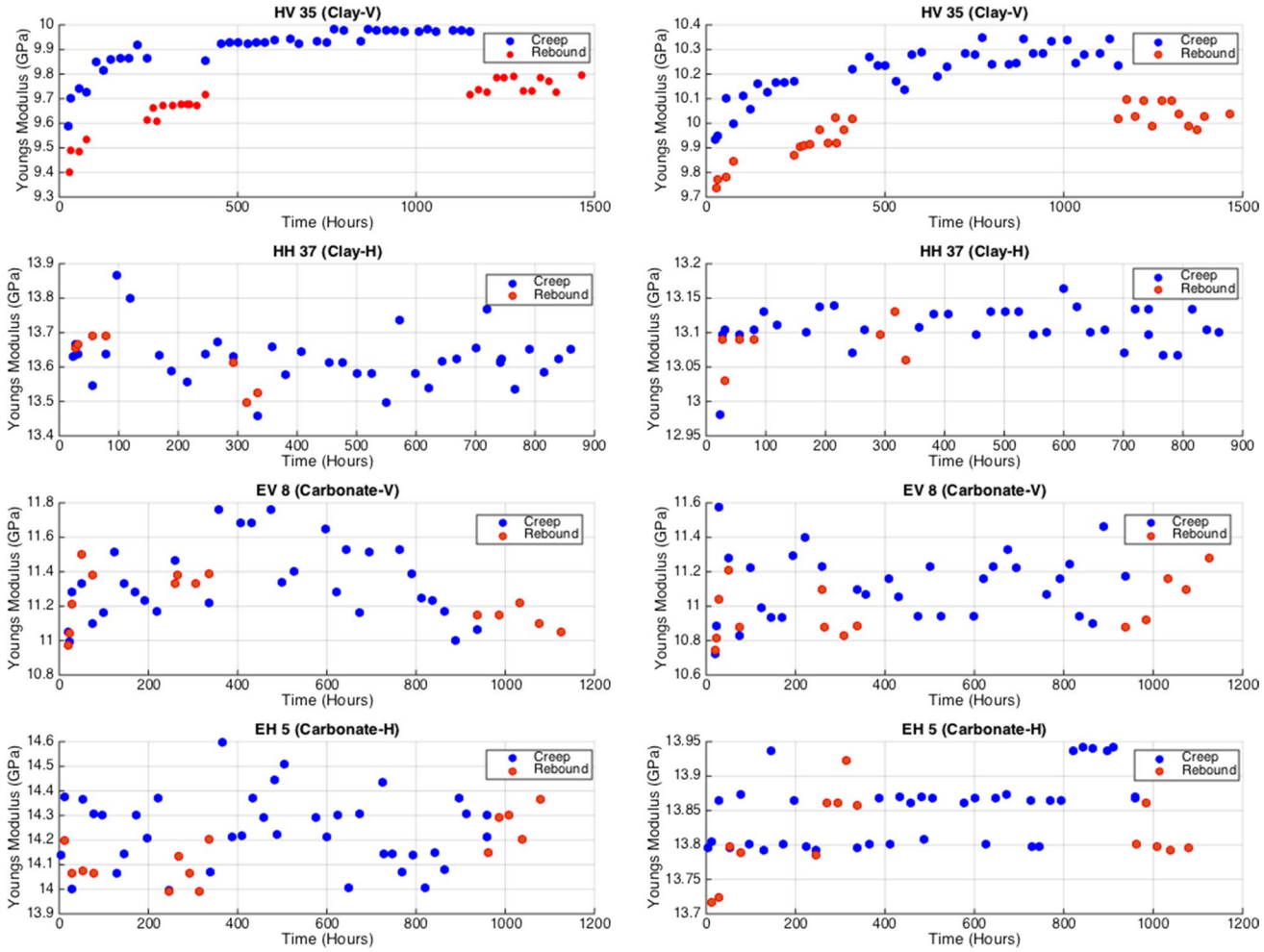

Fig. 19 Dynamic Young's modulus of the samples calculated from ultrasonic velocities. The two columns show *E* values calculated from two orthogonal S-waves

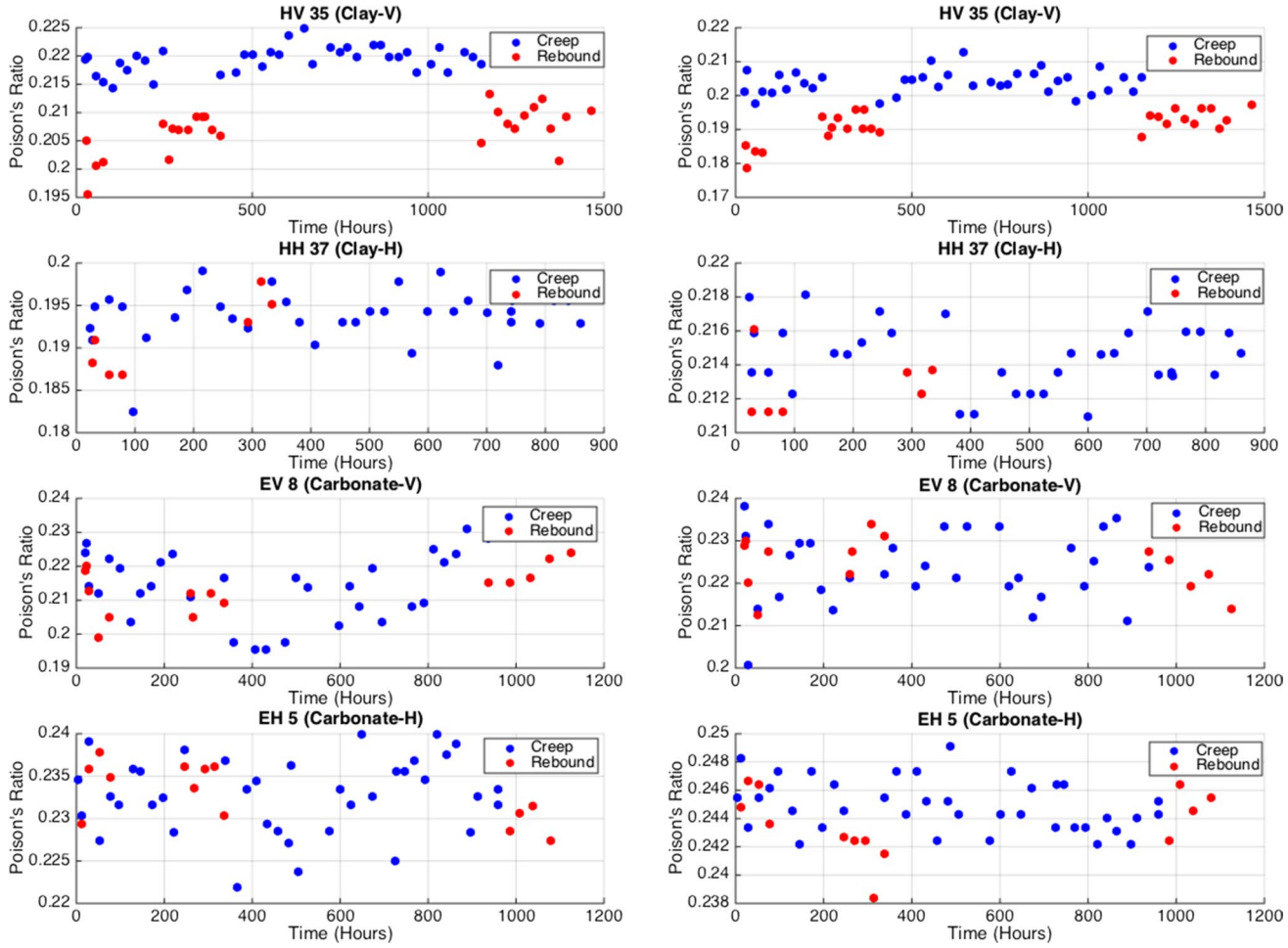

Fig. 20 Poisson's ratio of the samples calculated from ultrasonic velocities. The two columns show the Poisson's ratio calculated from two orthogonal S-waves

Both horizontal samples have higher dynamic E values and Poisson's ratio, which is in agreement with what we discussed above. The higher amount of Poisson's ratio shows that the horizontal samples are more expandable because of bedding planes parallel to the loading axis.

The small difference between the values calculated from horizontal and vertical S-waves depends on the position of the core holders with respect to the bedding planes. Since in these experiments we were not interested in S-wave anisotropy, we did not choose the orientation of piezoelectric crystals with respect to the orientation of bedding planes in the samples.

References

Bayuk I, Ammerman M, Chesnokov E (2007) Elastic moduli of anisotropic clay. Geophysics 72:D107–D117

Bernabe Y (1986) Pore volume and transport properties changes during pressure cycling of several crystalline rocks. Mech Mater 5(3):235–249

Boukharov G, Chanda M, Boukharov N (1995) The three processes of brittle crystalline rock creep. Int J Rock Mech Min Sci Geomech Abstr 32:325–335

Brace W, Paulding B, Scholz C (1966) Dilatancy in the fracture of crystalline rocks. J Geophys Res 71(16):3939–3953

Chaboche JL (1986) Time-independent constitutive theories for cyclic plasticity. Int J Plast 2(2):149–188

Chaboche J (2008) A review of some plasticity and viscoplasticity constitutive theories. Int J Plast 24(10):1642–1693

Chang C, Zoback MD (2010) Viscous creep in room-dried unconsolidated gulf of mexico shale (ii): development of a viscoplasticity model. J Pet Sci Eng 72(1):50–55

Cogan J (1976) Triaxial creep tests of opohonga limestone and ophir shale. Int J Rock Mech Min Sci Geomech Abstr 13:1–10

Croizé D, Renard F, Gratier J-P (2013) Compaction and porosity reduction in carbonates: a review of observations, theory, and experiments. Adv Geophys 54:181–238

Cuisiat F, Grande L, Heg K et al (2002) Laboratory testing of long term fracture permeability in shales. In: SPE/ISRM rock mechanics conference. Society of Petroleum Engineers

Davis NE, Kronenberg AK, Newman J (2008) Plasticity and diffusion creep of dolomite. Tectonophysics 456(3–4):127–146

Fan L, Martin RB, Thompson JW, Atwood K, Robinson JR, Lindsay GJ et al (2011) An integrated approach for understanding oil and gas reserves potential in eagle ford shale formation. In: Canadian unconventional resources conference. Society of Petroleum Engineers

Fan Z, Eichhubl P, Gale JF (2016) Geomechanical analysis of uid injection and seismic fault slip for the mw4. 8 timpson, texas, earthquake sequence. J Geophys Res Solid Earth 121(4):2798–2812

Ferrari A, Laloui L (2013) Advances in the testing of the hydro-mechanical behaviour of shales. In: Multiphysical testing of soils and shales. Springer, Berlin, pp 57–68

Fujii Y, Kiyama T, Ishijima Y, Kodama J (1999) Circumferential strain behavior during creep tests of brittle rocks. Int J Rock Mech Min Sci 36(3):323–337

Gasc-Barbier M, Chanchole S, Berest P (2004) Creep behavior of bure clayey rock. Appl Clay Sci 26(1):449–458

Goodman RE (1989) Introduction to rock mechanics, vol 2. Wiley, New York

Gratier JP, Guiguet R, Renard F, Jenatton L, Bernard D (2009) A pressure solution creep law for quartz from indentation experiments. J Geophys Res Solid Earth 114:B3

Hammes U, Hamlin HS, Ewing TE (2011) Geologic analysis of the upper jurassic Haynesville shale in east texas and west louisiana. AAPG Bull 95(10):1643–1666

Hatzor YH, Palchik V (1998) A microstructure-based failure criterion for Aminadav dolomites. Int J Rock Mech Min Sci 35(6):797–805

Horsrud P, Snsteb E, Be R (1998) Mechanical and petrophysical properties of North Sea shales. Int J Rock Mech Min Sci 35(8):1009–1020

Hyde T, Sun W, Hyde C (2013) An overview of small specimen creep testing. In: Altenbach H, Kruch S (eds) Advanced materials modelling for structures. Springer, Berlin, pp 201–216

Kennedy LA, White JC (2001) Low-temperature recrystallization in calcite: mechanisms and consequences. Geology 29(11):1027–1030

Khan AS, Farrokh B (2006) Thermo-mechanical response of nylon 101 under uniaxial and multi-axial loadings: Part I, experimental results over wide ranges of temperatures and strain rates. Int J Plast 22(8):1506–1529

Kias E, Maharidge R, Hurt R et al (2015) Mechanical versus mineralogical brittleness indices across various shale plays. In: SPE annual technical conference and exhibition. Society of Petroleum Engineers

Krempl E, McMahon J, Yao D (1986) Viscoplasticity based on overstress with a differential growth law for the equilibrium stress. Mech Mater 5(1):35–48

Kubetsky V, Eristov V (1970) In situ investigations of creep in rock for the design of pressure tunnel linings. British Geotechnical Society, pp 83–91

Kwon O, Kronenberg AK, Gangi AF, Johnson B, Herbert BE (2004) Permeability of illite-bearing shale: 1: Anisotropy and effects of clay content and loading. J Geophys Res Solid Earth 109(10):B10205-1

Lakes RS (2009) Viscoelastic materials. Cambridge University Press, Cambridge

Li W, Jin C, Salviato M, Cusatis G et al (2015) Modeling of failure behavior of anisotropic shale using lattice discrete particle model. In: 49th US rock mechanics/geomechanics symposium. American Rock Mechanics Association

Lockner D, Byerlee J (1977) Acoustic emission and creep in rock at high conning pressure and differential stress. Bull Seismol Soc Am 67(2):247–258

Lund Snee JE, Zoback MD (2016) State of stress in texas: implications for induced seismicity. Geophys Res Lett 43(19):10-208

Moore DE, Lockner DA (2004) Crystallographic controls on the frictional behavior of dry and water-saturated sheet structure minerals. J Geophys Res Solid Earth 109(B3). https://doi.org/10.1029/2003JB002582

Mullen J et al (2010) Petrophysical characterization of the eagle ford shale in south Texas. In: Canadian unconventional resources and international petroleum conference. Society of Petroleum Engineers

Murray RC (1960) Origin of porosity in carbonate rocks. J Sediment Res 30:59–84

Paterson MS, Wong TF (2005) Experimental rock deformation-the brittle field. Springer, The Netherlands

Pope C et al (2009) Haynesville shale-one operator's approach to well completions in this evolving play. In: SPE Annual Technical Conference and Exhibition. Society of Petroleum Engineers

Putnis A, Putnis CV (2007) The mechanism of reequilibration of solids in the presence of a fluid phase. J Solid State Chem 180(5):1783–1786

Rassouli F, Moosavi M, Jafari M et al (2009) The application of impression test in creep behavior of mudstone. In: ISRM regional symposium-eurock 2009. International Society for Rock Mechanics

Raufaste C et al (2011) The mechanism of porosity formation during solvent-mediated phase transformations. Proc R Soc London A: Math Phys Eng Sci 467(2129):1408–1426

Ruggles M, Krempl E (1990) The interaction of cyclic hardening and ratchetting for AISI type 304 stainless steel at room temperature—I. Experiments. J Mech Phys Solids 38(4):575–585

Ruiz-Agudo E, Putnis CV, Putnis A (2014) Coupled dissolution and precipitation at mineral-fluid interfaces. Chem Geol 383:132–146

Rutter E (1972) On the creep testing of rocks at constant stress and constant force. Int J Rock Mech Min Sci Geomech Abstr 9:191–195

Rybacki E, Reinicke A, Meier T, Makasi M, Dresen G (2015) What controls the mechanical properties of shale rocks?—Part I: strength and Young's modulus. J Pet Sci Eng 135:702–722

Sone H (2012) Mechanical properties of shale gas reservoir rocks, and its relation to the in situ stress variation observed in shale gas reservoirs, Ph.D. thesis, Stanford University

Sone H, Zoback MD (2013) Mechanical properties of shale-gas reservoir rocks Part 1: static and dynamic elastic properties and anisotropy. Geophysics 75:D381–D392

Sone H, Zoback MD (2014a) Time-dependent deformation of shale gas reservoir rocks and its long-term effect on the in situ state of stress. Int J Rock Mech Min Sci 69:120–132

Sone H, Zoback MD (2014b) Viscous relaxation model for predicting least principal stress magnitudes in sedimentary rocks. J Pet Sci Eng 124:416–431

Spain DR, Anderson GA (2010) Controls on reservoir quality and productivity in the Haynesville shale, vol 60. Gulf coast association of geological societies transactions, Northwestern gulf of mexico basin, pp 657–668

Thompson J, Fan L, Grant D, Martin RB, Kanneganti KT, Lindsay GJ et al (2011) An overview of horizontal-well completions in the Haynesville shale. J Can Pet Technol 50(06):22–35

Van Oort E (2003) On the physical and chemical stability of shales. J Pet Sci Eng 38(3):213–235

Wawersik W, Brace W (1971) Post-failure behavior of a granite and diabase. Rock Mech 3(2):61–85

Yang Y, Zoback M (2016) Viscoplastic deformation of the Bakken and adjacent formations and its relation to hydraulic fracture growth. Rock Mech Rock Eng 49(2):689–698

Yang Y, Sone H, Zoback M et al (2015) Fracture gradient prediction using the viscous relaxation model and its relation to out-of-zone microseismicity. In: SPE annual technical conference and exhibition. Society of Petroleum Engineers

Yoshida F (1990) Uniaxial and biaxial creep-ratcheting behavior of SUS304 stainless steel at room temperature. Int J Press Vessels Pip 44(2):207–223

Zhang CL, Rothfuchs T, Su K, Hoteit N (2007) Experimental study of the thermo-hydro- mechanical behaviour of indurated clays. Phys Chem Earth A/B/C 32(8):957–965

Zhu W, Baud P, Wong TF (2010) Micromechanics of cataclastic pore collapse in limestone. J Geophys Res Solid Earth 115(B4). https://doi.org/10.1029/2009JB006610